



Cite this: DOI: 10.1039/c9cc08493b

Received 31st October 2019,
Accepted 9th December 2019

DOI: 10.1039/c9cc08493b

rsc.li/chemcomm

The coinciding effects of carbon defects and oxygen functional groups in porous graphene were demonstrated in this work. The species and distributions of oxygen functional groups evolved with the types of defects, especially those containing C=O bonds mainly distributed along the edge of ring defects, and enhanced Na⁺ storage.

The production of lithium-ion batteries (LIBs) is in large part responsible for the massive consumption of limited lithium reserves. The revival of sodium-ion batteries (SIBs) is considered to be a promising option to alleviate this issue owing to the abundant supply and low cost of sodium. Carbon materials are regarded as the ideal anode candidates for SIBs given their virtues of high abundance, good electrical conductivity and high chemical stability.¹ The main challenges facing carbon materials are the sluggish diffusion kinetics and scanty Na⁺ reactive sites, which are responsible for their inferior electrochemical properties and greatly hinder their practical applications.

Introducing carbon defects could, due to the high reactivity of exposed edge carbon atoms, efficiently activate the diffusion of ions and provide additional reactive sites.² Doping carbon materials with heteroatoms (e.g., B, N, P, S) has garnered much attention as this process breaks the integrity of the carbon π electron system, and generates structural defects that can accommodate the dopant atoms.^{1,3} A considerable amount of research has been devoted to introducing carbon defects through various strategies and to investigating the effects of intrinsic carbon defects on Na⁺ storage activities. However, there are many types of carbon defects, and importantly, oxygen functional groups

Defect formation-induced tunable evolution of oxygen functional groups for sodium storage in porous graphene[†]

Jianqi Ye,^{‡,a} Hanqing Zhao,^{‡,†,a} Mengmeng Kang,^a Wei Song,^a Qingqiang Kong,^b Chengmeng Chen,^{‡,b} Rui Wu,^c Jie Mi^a and Zhong Li^{‡,a}

are ubiquitous and tend to distribute on the edges of carbon material defects.^{4,5} Considering that the Na⁺ storage capability and electronic structure of oxygen functional groups vary in each species, the evolution of oxygen functional groups occurring along defects will make a difference to the adsorption and diffusion of Na⁺.^{6,7} To the best of our knowledge, the effect of intrinsic carbon defect types on the evolution of oxygen functional groups has not yet been investigated. Exploring the interplay between carbon defect types and oxygen functional groups is therefore highly needed.

Herein, three-dimensional graphene, a widely studied building block for sp² carbon allotropes, was selected as the starting carbon material. Our results demonstrated that the species and distributions of oxygen functional groups evolved with the introduction of different types of defects, and that ring defects may be responsible for the distribution of groups containing C=O bonds. The generated pores promoted cross-plane mobility of Na⁺, and defects along the pores appeared to have provided additional Na⁺ storage active sites, endowing the material with enhanced electrochemical properties, in particular a specific capacity of 153.5 mA h g⁻¹ at 2 A g⁻¹. The presented work revealed the interplay between carbon defect types and oxygen functional groups, and their contributions to the electrochemical properties, which have extensive implications for the design of defect-containing carbon electrodes.

The porous graphene (PG) was prepared using a metal etching method and the corresponding procedure is depicted in Fig. S1a in the ESI.[†] The metal atoms (iron, nickel and cobalt) acted as nucleation sites to snatch carbon atoms from the graphene, and form graphene-adhered nanoparticles with different sizes under calcination.⁸ Afterwards, the nanosized in-plane pores and accompanying defects were generated after removing the metal nanoparticles.^{9,10} Inspection of TEM images of these graphene materials (Fig. S1d-f, ESI[†]) confirmed the presence of nanopores in them, with average pore size (D_{avg}) values for Co-PG, Ni-PG and Fe-PG estimated to be 22, 35, and 42 nm, respectively. This trend was found to be similar to that for the particle sizes of metal species on the graphene as

^a Key Laboratory of Coal Science and Technology of Ministry of Education and Shanxi Province, Institute of Coal Chemical Engineering, Taiyuan University of Technology, Taiyuan 030024, Shanxi, China. E-mail: zhaohanqing@tyut.edu.cn, lizhong@tyut.edu.cn

^b CAS Key Laboratory of Carbon Materials, Institute of Coal Chemistry, Chinese Academy of Sciences, Taiyuan 030001, China

^c Beijing Synchrotron Radiation Facility, Institute of High Energy Physics, Chinese Academy of Sciences, Beijing 100049, P. R. China

[†] Electronic supplementary information (ESI) available. See DOI: 10.1039/c9cc08493b

[‡] These authors contribute equally to this work.

determined from the inspection of the corresponding SEM images (Fig. S1g–i, ESI†).

XRD patterns of the samples each showed two peaks characteristics of the (002) and (100) carbon planes (Fig. S2a, ESI†). The peak width at half maximum (FWHM) values of the Co-PG (0.780), Ni-PG (0.801), and Fe-PG (0.898) samples were observed to be greater than that of graphene (0.670), evidence for their having more defects and deteriorated carbon lattices. Raman spectra were also acquired to evaluate the extent of defects in the samples (Fig. S2b, ESI†); here the ratio of the integrated intensity of the D peak to that of the G peak (I_D/I_G) in each fitting spectrum was used to quantify the concentration of defects. The porous graphene materials showed higher I_D/I_G values than did graphene, suggesting that more defects formed along the pores, and that the degree of disorder increased with the pore size in the graphene. The N_2 adsorption–desorption isotherms of the samples showed typical IV curve shapes with hysteresis loops (Fig. S2c, ESI†), indicating the co-existence of micropores and mesopores. Moreover, the surface area of porous graphene increased accordingly with the generated pore size, and the specific surface areas were estimated to be 151.3, 234.2 and $263.4\text{ m}^2\text{ g}^{-1}$ for the Co-PG, Ni-PG and Fe-PG samples, respectively, all greater than the $141.7\text{ m}^2\text{ g}^{-1}$ specific surface area of graphene. The pore width distributions of all of the samples were mainly centered about a value of 3.37 nm (Fig. S2d, ESI†), and the differences between the pore sizes determined from TEM images and those from N_2 adsorption–desorption analysis were mainly attributed to the limited quantity of generated pores compared to the quantity of original corners in the 3D-graphene.

The chemical states and structural features of the samples were characterized by acquiring their XANES spectra. At the C K-edge, the XANES spectra displayed three main features, at 285.7, 288.7 and 292.1 eV (Fig. 1a), labeled as A, B, C, respectively. Features A and C can be assigned to the excitations of the C–C π^* and σ^* states in the hexagonal graphite sheets.¹¹ Feature B was associated with the $1s \rightarrow \pi^*$ resonances from oxygen functional groups containing C=O bonds, which could serve as the reactive sites and benefit Na⁺ storage.^{7,12} The shoulder in the spectrum at around 284.5 eV (inset) corresponded to the edge states appearing at the zigzag edge of graphite; note that it became weaker after pores formed, indicating the decreased concentration of edge defects.¹² This result may be attributed to the reconstruction of remaining carbon atoms resulting from the reaction between metal atoms and carbon atoms consuming some of the oxygen functional groups on the graphene during the thermal treatment.^{13,14} As seen upon comparing the Co-PG, Ni-PG, and Fe-PG XANES spectra, the intensity of peak A clearly weakened with increasing pore size, suggesting that the carbon network was destroyed and hence that more structural defects formed during the pore formation,¹⁵ consistent with the Raman analysis. Moreover, feature C corresponding to the C–C σ^* states at 292.1 eV shifted to lower energy upon converting graphene to Fe-PG (inset), evidence for an increase in the quantity of carbon defects in the sp^2 rings.¹² These results illustrated that the intensification of the Raman D-band was mainly caused by an increase in the concentration of ring defects

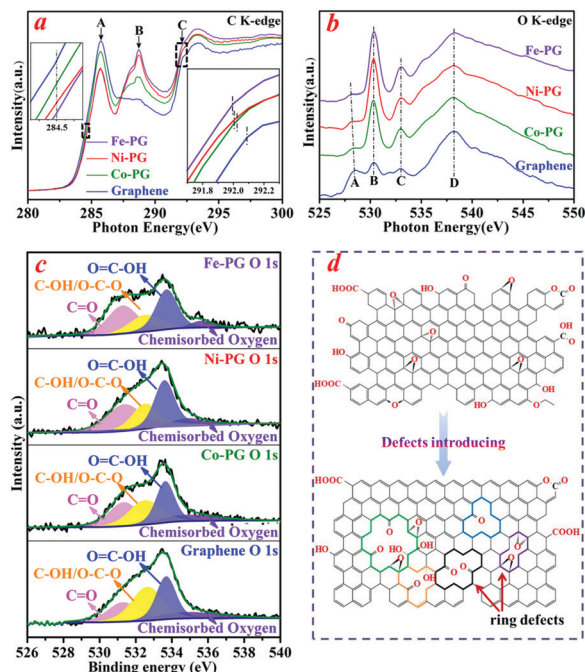


Fig. 1 (a and b) XANES spectra at (a) the C K-edge and (b) O K-edge. (c) XPS spectra, in the O 1s region, of all of the samples. (d) Schematic diagram of the evolution of oxygen functional groups upon introducing defects.

rather than edge defects. The corresponding differences in feature B suggested that the oxygen groups including C=O bonds were mainly present on the ring defects along the pores.⁵

Four dominant features were detected at the O K-edge of each XANES spectrum (Fig. 1b). Feature A located at 528.4 eV for graphene was apparently due to the pre-edge peak of carbonyl-type functional groups.¹⁶ Interestingly, the peak shifted to lower excitation energies upon the formation of the pores and its intensity was weaker for Fe-PG than for Co-PG, which might have been due to differences in oxygen atom bonding and oxygen group evolution.¹⁶ Features denoted as B, C and D centered at 530.3, 532.9 and 538.2 eV can be assigned to the π^* resonance of C=O bonds, O–H σ^* states in basal phenolic groups and the C–O σ^* transitions in various C–O groups, respectively.¹⁷ The intensities of features B and C exhibited a trend opposite that exhibited by feature A, and increased with the pore size, and thus we conjectured that some oxygen functional groups transformed to those containing C=O bonds during the introduction of carbon defects.

XPS survey spectra revealed lower amounts of O after defects were introduced, with values of 4.4, 3.3, 3.7 and 3.0 at% for the graphene, Co-PG, Ni-PG and Fe-PG samples, respectively (Fig. S3, ESI†). These results were due to the consumption of oxygen groups during the metal etching treatment. XPS spectra in the C 1s region (Fig. S4, ESI†) showed that the peak at 284.6 eV, corresponding to C=C/C–C, was weakened after the deterioration of the carbon π conjugated system and introduction of carbon defects. In good agreement with the XANES analysis, the XPS spectra in the O 1s region showed that the quantity of C=O groups, which could act as the reactive sites and promote

Na^+ adsorption, increased upon the introduction of defects (Fig. 1c). The relative amounts of $\text{C}-\text{OH}/\text{O}-\text{C}-\text{O}$ groups followed a trend opposite that for the $\text{C}=\text{O}$ groups, attributed to the $\text{C}-\text{O}$ bond energy being weaker and thus the $\text{C}-\text{O}$ bonds being easier to break. Note that there were no extra oxygen functional groups imported during the synthesis of porous graphene. Therefore, the increased ratio of the amount of $\text{C}=\text{O}$ to that of $\text{C}-\text{OH}/\text{O}-\text{C}-\text{O}$ revealed that the introduced carbon defects could cause a local electronic redistribution, and endow the charge densities of the carbon matrix with a better oxygen affinity, resulting in the evolution of oxygen functional groups as depicted in Fig. 1d.² Yet, further investigation of a detailed mechanism still needs to be carried out.

TG-MS spectra were acquired to accurately evaluate the oxygen functional groups in the carbon framework according to the differences between the thermal stabilities of various species of oxygen groups (Fig. 2a-d).^{18,19} The relative amount of groups with $\text{C}=\text{O}$ bonds for the Ni-PG sample was higher than that for graphene, while the relative amount of $\text{C}-\text{O}$ bonds was lower, conclusions coincident with those from the XANES and XPS analyses, and further supporting the hypothesis that oxygen functional groups evolved during the introduction of defects (Fig. 2e). Additionally, due to the tendency of the carboxyl groups to distribute along the edge sites of graphene, the decreased relative amounts of carboxyl groups in the Ni-PG sample reflected its lower content of edge defects, as the XANES study revealed.²⁰

The initial three cycles of the CV curves of Ni-PG are presented in Fig. 3a. An intense peak at 0.8 V corresponded to the decomposition of electrolyte and the formation of solid electrolyte

interface layer in the first cathodic scan, and it disappeared in the subsequent cycles, illustrating that such irreversible reactions mainly occurred in the first cycles. Significantly, the CV patterns overlapped well in the following cycles, indicating the good reversibility of the Ni-PG electrode. A pair of redox peaks appeared at 2.3/2.2 V after the first cycle, attributed to the reversible reaction of Na^+ with the exposed defect sites and the surface oxygen functional groups.²¹ Additionally, the sharp redox peaks centered at 0.01 V can be related to the intercalation/deintercalation of Na^+ .

The cycling properties of the samples were evaluated at 2 A g^{-1} after activation of the electrodes at 0.05 A g^{-1} for the initial five cycles (Fig. 3b). The Ni-PG electrode delivered the best cycling performance, with a specific capacity of 153.5 mA h g^{-1} after 160 cycles, higher than the 141.5, 136 and 124 mA h g^{-1} values for Co-PG, Fe-PG and graphene, respectively. Note that the rate capabilities of porous graphene were to various degrees better than that of the graphene electrode (Fig. 3c). For the Ni-PG sample, specific capacities of 261.6, 251.1, 248.7, 225.1, 202.1 and 174.4 mA h g^{-1} were achieved at current densities of 0.05, 0.1, 0.2, 0.5, 1, and 2 A g^{-1} , respectively. When the current density was decreased back to 0.05 A g^{-1} , the capacity was observed to be 282.3 mA h g^{-1} , achieving a capacity improvement of 27% compared to that of graphene. The capacity increase trend may be attributed to the electrode activation effect involving the reversible formation of a conductive gel-like film on the electrode surface induced by the decomposition of electrolyte, and to the greater number of sodium storage active sites (*i.e.*, defects and oxygen functional groups) exposed during cycling.^{22,23} The high electrochemical performance of Ni-PG, best of the samples tested, can be attributed to its moderate pore size, the synergistic effects of its defects and oxygen functional groups, and its increased quantity of $\text{C}=\text{O}$ bonds that acted as the sodium storage sites and boosted its Na^+ storage kinetics. EIS measurements were taken to gain insight into the reaction kinetics of the samples. The charge transfer resistance (R_{ct}) values were calculated, based on the fitted equivalent electric circuits, to be 7.72, 10.36, 15.49 and 17.69 Ω for graphene, Co-PG, Ni-PG and Fe-PG, respectively (Fig. 3d). The slightly increased R_{ct} here,

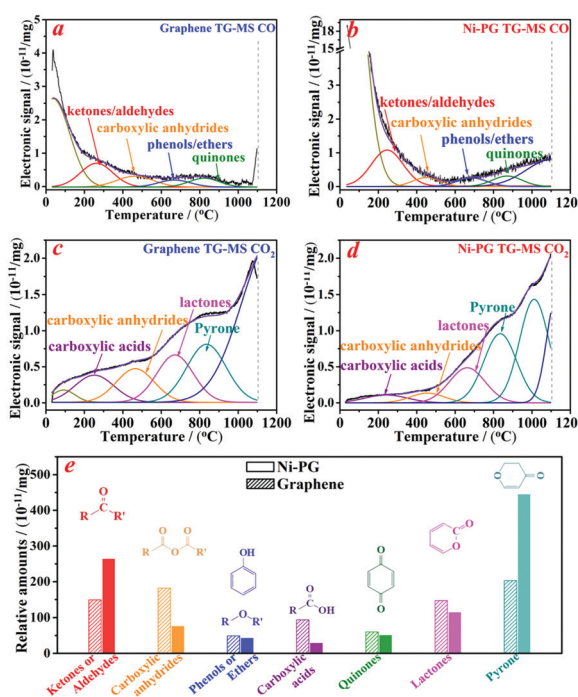


Fig. 2 (a-d) TG-MS spectra showing (a and b) CO and (c and d) CO_2 evolution profiles of (a and c) graphene and (b and d) Ni-PG samples, and (e) their relative amounts of oxygen functional groups.

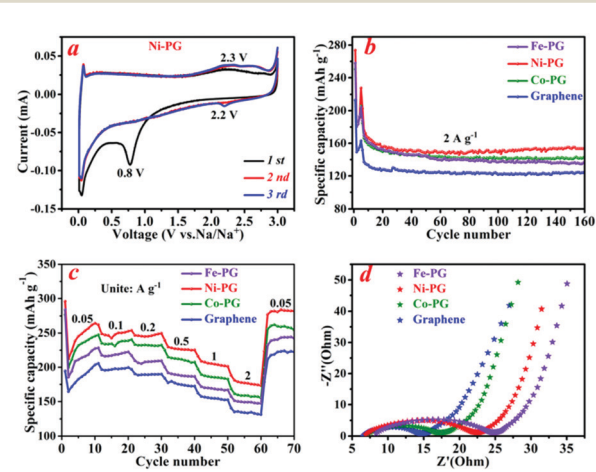


Fig. 3 (a) CV profile of Ni-PG. (b) Cycling performances at 2 A g^{-1} , (c) rate performances, and (d) EIS analyses of all of the samples.

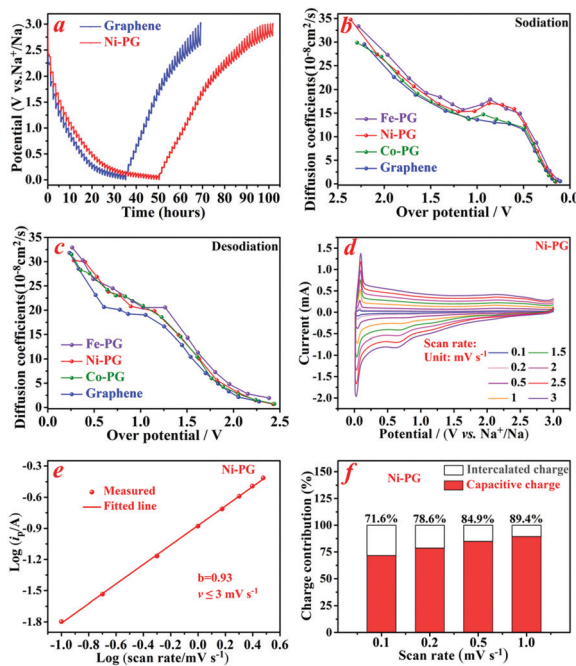


Fig. 4 (a) GITT curves of Ni-PG and graphene. (b and c) Calculated diffusion coefficients during (b) sodiation and (c) desodiation. (d) CV curves, (e) b value, and (f) capacitive contribution ratios of Ni-PG.

i.e., inferior of electronic conductivity, was apparently due to the defect-induced deterioration of the carbon π conjugated system.

The GITT technique (Fig. 4a and Fig. S5, ESI[†]) was applied to evaluate the kinetics of the electrodes, and the diffusion coefficients of Na⁺ transport (D_{Na}) in the various electrodes were estimated using the equation

$$D = 4((mV_M)/(MS))^2((\Delta E_s)/(\Delta E_v))^2/\pi\tau. \quad (1)$$

The D_{Na} values of the porous graphene samples were in this way determined to be higher than that of graphene during the charge/discharge process (Fig. 4b and c) and to display a trend identical to the trend of pore sizes. These results can be ascribed to the shortened Na⁺ diffusion path afforded by the generated pores and the weakened steric-hindrance effect of oxygen-containing groups contributing to the Na⁺ storage kinetics and rate capability.²⁴ CV curves at various scan rates from 0.1 to 3 mV s⁻¹ were acquired to gain insight into the sodium storage mechanism of Ni-PG (Fig. 4d). A b value (0.93, Fig. 4e) approaching 1 was calculated based on the equation $i = av^b$, implying a process driven by surface capacity owing to the increased quantities of defects and reactive oxygen groups. The capacitive contribution ratios were determined using the equation $i = k_1v + k_2v^{1/2}$; this ratio was found to increase with the sweep rate and to reach 89.4% at 1 mV s⁻¹, indicating the critical role played by the adsorption process in high-current conditions (Fig. 4f).¹

To conclude, the porous graphene samples with different pore sizes have been demonstrated as SIB anodes. The results showed that the formation of certain types of defects on graphene

could induce the evolution of oxygen functional groups, and the ring defects were predicted to be more pivotal than the edge defects to the electrochemical performance, and to be responsible for the distribution of oxygen groups with C=O bonds. Considering the wide usage of graphene, we expect the results of the present study to offer important insights into the optimization of carbon defects and oxygen functional groups, and to the rational design of defect-containing carbon materials in the energy field.

This work was supported by the Youth Foundation (201701D221070), Key Research and Develop Plan (International scientific and technological cooperation projects, 201803D421011) and Major Projects (MC2015-04) of Shanxi Province.

Conflicts of interest

There are no conflicts to declare.

Notes and references

- H. Hou, X. Qiu, W. Wei, Y. Zhang and X. Ji, *Adv. Energy Mater.*, 2017, 7, 1602898.
- J. Zhu, Y. Huang, W. Mei, C. Zhao, C. Zhang, J. Zhang, I. S. Amiuu and S. Mu, *Angew. Chem., Int. Ed.*, 2019, 58, 3859–3864.
- Y. Jiang, L. Yang, T. Sun, J. Zhao, Z. Lyu, O. Zhuo, X. Wang, Q. Wu, J. Ma and Z. Hu, *ACS Catal.*, 2015, 5, 6707–6712.
- D. Luo, J. Xu, Q. Guo, L. Fang, X. Zhu, Q. Xia and H. Xia, *Adv. Funct. Mater.*, 2018, 28, 1805371.
- Z. Liu, L. Jiang, L. Sheng, Q. Zhou, T. Wei, B. Zhang and Z. Fan, *Adv. Funct. Mater.*, 2018, 28, 1705258.
- A. C. Ferrari and D. M. Basko, *Nat. Nanotechnol.*, 2013, 8, 235–246.
- M. Kang, H. Zhao, J. Ye, W. Song, H. Shen, J. Mi and Z. Li, *J. Mater. Chem. A*, 2019, 7, 7565–7572.
- J. Du, F. Cheng, S. Wang, T. Zhang and J. Chen, *Sci. Rep.*, 2014, 4, 4386.
- X. Zhang, J. Zhou, C. Liu, X. Chen and H. Song, *J. Mater. Chem. A*, 2016, 4, 8837–8843.
- H. Cao, X. Zhou, C. Zheng and Z. Liu, *Carbon*, 2015, 89, 41–46.
- L. Ji, M. Rao, H. Zheng, L. Zhang, Y. Li, W. Duan, J. Guo, E. J. Cairns and Y. Zhang, *J. Am. Chem. Soc.*, 2011, 133, 18522–18525.
- W. Wang, L. Shang, G. Chang, C. Yan, R. Shi, Y. Zhao, G. I. N. Waterhouse, D. Yang and T. Zhang, *Adv. Mater.*, 2019, 31, 1808276.
- Y. Jia, L. Zhang, A. Du, G. Gao, J. Chen, X. Yan, C. L. Brown and X. Yao, *Adv. Mater.*, 2016, 28, 9532–9538.
- J. Gao, Y. Wang, H. Wu, X. Liu, L. Wang, Q. Yu, A. Li, H. Wang, C. Song, Z. Gao, M. Peng, M. Zhang, N. Ma, J. Wang, W. Zhou, G. Wang, Z. Yin and D. Ma, *Angew. Chem., Int. Ed.*, 2019, 131, 15233–15241.
- Y. Gao, G. Hu, J. Zhong, Z. Shi, Y. Zhu, D. S. Su, J. Wang, X. Bao and D. Ma, *Angew. Chem., Int. Ed.*, 2013, 52, 2109–2113.
- K. Kim, P. Zhu, N. Li, X. Ma and Y. Chen, *Carbon*, 2011, 49, 1745–1751.
- J. Zhong, J. Deng, B. Mao, T. Xie, X. Sun, Z. Mou, C. Hong, P. Yang and S. Wang, *Carbon*, 2012, 50, 335–338.
- G. S. Szymanski, Z. Karpinski, S. Biniak and A. Swiatkowskic, *Carbon*, 2002, 40, 2627–2639.
- J. Xu, J. Zhao, J. Xu, T. Zhang, X. Li, X. Di, J. Ni, J. Wang and J. Cen, *Ind. Eng. Chem. Res.*, 2014, 53, 14272–14281.
- I. Y. Jeon, Y. R. Shin, G. J. Sohn, H. J. Choi, S. Y. Bae, J. Mahmood, S. M. Jung, J. M. Seo, M. J. Kim, D. Wook Chang, L. Dai and J. B. Baek, *Proc. Natl. Acad. Sci. U. S. A.*, 2012, 109, 5588–5593.
- G. Zou, H. Hou, G. Zhao, Z. Huang, P. Ge and X. Ji, *Green Chem.*, 2017, 19, 4622–4632.
- J. Ruan, T. Yuan, Y. Pang, S. Luo, C. Peng, J. Yang and S. Zheng, *Carbon*, 2018, 126, 9–16.
- M. Wang, Z. Yang, W. Li, L. Gu and Y. Yu, *Small*, 2016, 12, 2559–2566.
- Y. Wen, K. He, Y. Zhu, F. Han, Y. Xu, I. Matsuda, Y. Ishii, J. Cumings and C. Wang, *Nat. Commun.*, 2014, 5, 4033.